Article:
Li, W., Cai, J., Yan, Y. et al. (11 more authors) (2018) Correlating three-dimensional morphology with function in PBDB-T:IT-M non-fullerene organic solar cells. Solar RRL, 2 (9). 1800114. ISSN 2367-198X

https://doi.org/10.1002/solr.201800114

Correlating three-dimensional morphology with function in PBDB-T:IT-M non-fullerene organic solar cells

Wei Li[1], Jinlong Cai[1], Yu Yan[1], Feilong Cai[1], Sunsun Li[2], Robert S. Gurney[1], Dan Liu[1], James D. McGettrick[3], Trystan M. Watson[3], Zhe Li[4], Andrew J. Pearson[5], David G. Lidzey[6], Jianhui Hou[2], Tao Wang[1]*

[1]School of Materials Science and Engineering, Wuhan University of Technology, Wuhan 430070, China E-mail: twang@whut.edu.cn

[2]State Key Laboratory of Polymer Physics and Chemistry, Institute of Chemistry, Chinese Academy of Sciences

[3]SPECIFIC, College of Engineering, Bay Campus, Swansea University, Swansea, SA1 8EN, UK

[4]School of Engineering, Cardiff University, Cardiff, Wales UK, CF24 3AA

[5]Cavendish Laboratory, University of Cambridge, J. J. Thomson Avenue, Cambridge CB3 0HE, UK

[6]Department of Physics and Astronomy, University of Sheffield, Sheffield S3 7RH, UK

Abstract: In this work, the correlation between three-dimensional morphology and device performance of PBDB-T:IT-M non-fullerene organic solar cells was investigated. We found that a PBDB-T-rich top layer formed when the PBDB-T:IT-M film was cast on PEDOT:PSS, indicating a vertical component distribution that will hinder electron transport towards the cathode in a conventional device. This PBDB-T-rich top layer remained upon low-temperature annealing at 80 ^{o}C, but disappeared when the annealing temperature was raised, resulting in an optimum annealing temperature of 160 ^{o}C for conventional devices as the removal of this polymer-rich layer facilitates electron transport toward the top cathode layer. The PBDB-T-rich layer was also found in the surface region of PBDB-T:IT-M films cast on a TiO_2 substrate, but in this case it remained after thermal annealing at 80 or 160 ^{o}C, leading to a favorable vertical stratification for efficient charge collection in inverted devices. Although thermal annealing can enhance the crystallinity of this PBDB-T:IT-M blend and lead to improved charge mobility, the correlation length of the PBDB-T component increased excessively under annealing at 160 ^{o}C. Further, the packing of IT-M clusters became loose upon high temperature annealing, an effect we believe results in more diffuse interfaces with PBDB-T that result in reduced charge separation efficiency, consequently reducing the short-circuit current in the inverted devices.

Key words: Non-fullerene, Organic solar cells, Morphology, Vertical stratification

1. Introduction

Over the past few years, organic photovoltaics (OPVs) employing non-fullerene, n-type small molecular acceptors have achieved significant progress benefiting from their tunable optical properties and electronic energy levels compared to conventional fullerene acceptors[1-4]. Presently, the power conversation efficiency (PCE) of non-fullerene OPVs has exceeded 13% in binary single-junction devices[5], passed 14% in ternary single-junction devices[6,7], and is approaching 15% in tandem devices[8]. Non-fullerene acceptors (NFA) have demonstrated a bright future and have promising prospects to further promote and revolutionize the development of OPVs.

Similar to fullerene-based OPVs, the active layer of NFA-based OPVs is also fabricated by casting solutions with mixed electron-donors and electron-acceptors. However, in NFA-based OPVs the driving force required for efficient exciton dissociation at the donor-acceptor interface has been lowered considerably, which has led to reduced open-circuit voltage losses[9]. It is well accepted that the nanoscale morphology of NFA-based OPVs plays a significant role in determining the device metrics and efficiency[10-12]. The morphology of the photovoltaic blends of OPVs can be divided into two parts[13]. The first part is the nanoscale morphology in the lateral direction, when characterized this typically gives insight into molecular order and phase-separation between donor and acceptor domains[14-16]. The second part relates to vertical component distribution (i.e. vertical stratification) in the cross-section of photovoltaic blend films. [17-19] Whilst phase separation and molecular order are regularly discussed in the context of all aspects of photocurrent generation[20], vertical stratification is more closely associated with the transport of charge carriers from the bulk of the photoactive layer to the device electrodes[21].

Non-fullerene OPVs employing the conjugated polymer PBDB-T as donor and the n-type organic molecule IT-M as acceptor have for the first time achieved a PCE over 12% in single-junction solar cell devices[22,23]. Even though recent works have investigated the multi-length scale morphology and the thermodynamic drivers and kinetic trapping during the processing of non-fullerene OPVs[24,25], the vertical component distributions in as-cast non-fullerene photovoltaic blend-films subjected to post-deposition treatments have not yet been reported. In fullerene-based OPVs, non-uniform donor or acceptor distributions in the vertical direction of the photoactive layer, with polymer-rich or fullerene-rich sublayers formed near the top surfaces or buried interfaces with substrates, have been widely reported[26-28]. This vertical stratification can be altered by a number of

factors including: thermodynamics, kinetics, selective dissolubility and the surface free energies of materials and substrates[13,29]. For PBDB-T:IT-M solar cells a comprehensive understanding between the nanoscale morphology in three dimensions and photovoltaic function is still missing. The complete characterization of the morphology in both lateral and vertical directions of non-fullerene PBDB-T:IT-M bulk heterojunction active layers is therefore highly desired.

In this work, we have utilized synchrotron-based grazing incidence small-angle and wide-angle X-ray scattering (that is, GISAXS and GIWAXS) and X-ray photoelectron spectroscopy (XPS) with an etching technique to unravel the three-dimensional morphology of this high efficiency PBDB-T:IT-M photovoltaic system. The effect of thermal annealing, a post-deposition treatment that has been found to impact on device performance, on the molecular ordering, correlation length, and vertical stratification were characterized in detail. Conventional and inverted devices were fabricated to investigate the correlation between three-dimensional morphology and optoelectronic and photovoltaic functions of PBDB-T:IT-M OPVs. Various electrical measurements were also performed to examine the effect of morphology on exciton dissociation, charge transport and recombination. Our results not only extend our understanding of the nanoscale morphology of the PBDB-T:IT-M active layer in the vertical direction, but also explain the contrasting photovoltaic performance of conventional and inverted PBDB-T:IT-M OPVs upon different annealing temperatures, providing a guideline in further optimizing the nanomorphology of PBDB-T:IT-M OPVs and similar non-fullerene OPV systems.

2. Results and discussion

The chemical structures of electron-donor PBDB-T and electron-acceptor IT-M are shown in Figure 1a and b. In order to investigate the effects of three-dimensional morphology on device performance, we fabricated PBDB-T:IT-M OPVs in both conventional and inverted configurations by spin casting the PBDB-T:IT-M solution at a blending ratio of 1:1 on PEDOT:PSS and TiO_2 substrates, followed by applying a Ca/Ag or MoO_3/Ag bilayer via thermal evaporation. The top surfaces of the PBDB-T:IT-M photoactive layer are therefore adjacent to the cathode and anode layers in the conventional and inverted devices respectively. The energy level diagrams of conventional and inverted devices are shown in Figure 1c and d. Thermal annealing at a low temperature of 80 ^{o}C and a relatively high temperature of 160 ^{o}C are applied, as both temperatures have been reported as the optimum annealing temperature for non-fullerene based OPVs[22,23,30].

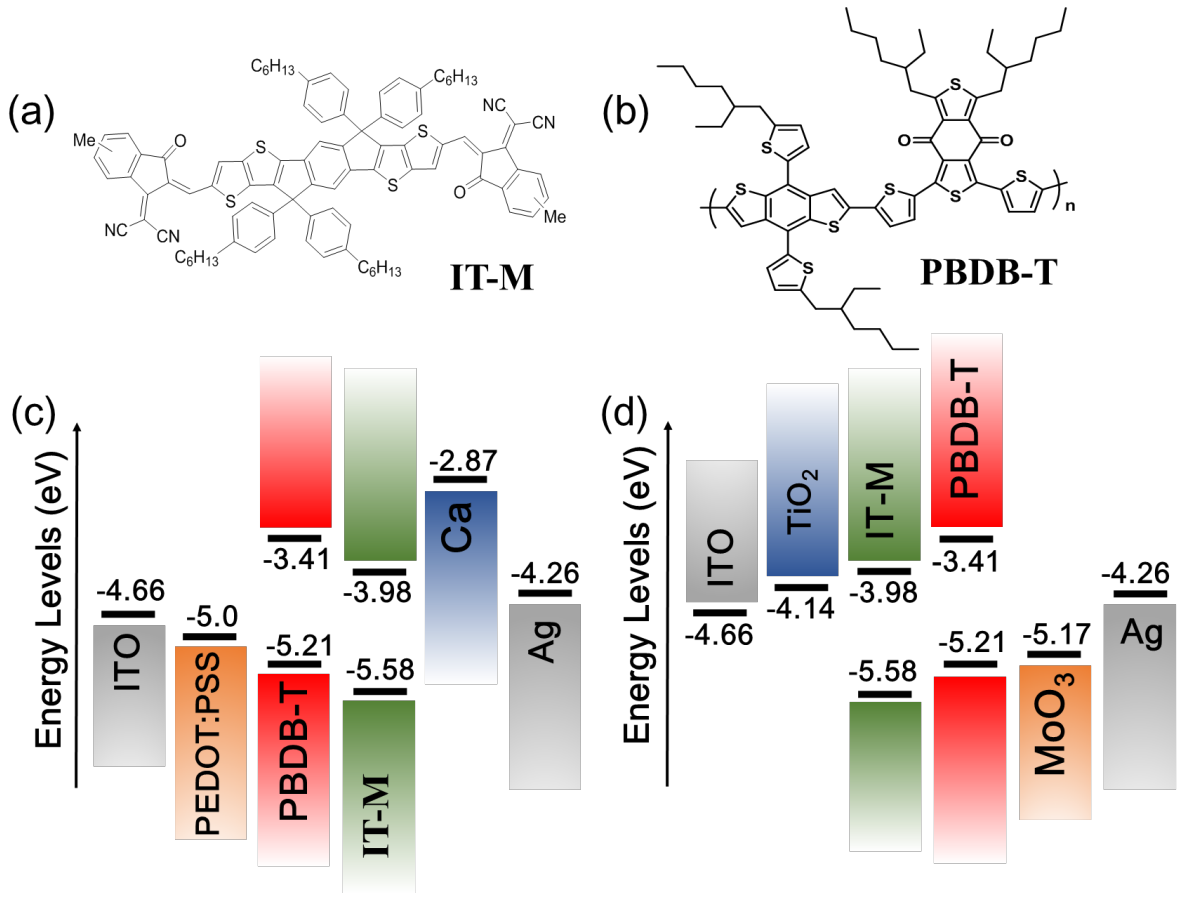

Figure 1 The chemical structures of (a) PBDB-T and (b) IT-M. Energy level diagrams of (c) conventional and (d) inverted devices.

We start with an examination of crystallization and domain changes in PBDB-T:IT-M films. Scanning probe microscopy (SPM) images of PBDB-T:IT-M films on PEDOT:PSS and TiO_2 substrates in an as-cast state or after thermal annealing at 80 and 160 ºC for 30 mins are shown in Figure S1. From Figure S1 we have observed very similar surface textures and roughness in all these films, without seeing excessive clusters when the blends were annealed at a relatively high-temperature of 160 ºC, a phenomenon in contrast to fullerene-based OPV blends where large domains will form as a result of diffusion and aggregation of PCBM nanoparticles. [31,32] We have therefore used GIWAXS and GISAXS to characterize our films. The 2D GIWAXS patterns of PBDB-T:IT-M in an as-cast state and after thermal annealing at 80 and 160 ºC for 30 mins are shown in Figure 2a-c, with 1D profiles in the in-plane and out-of-plane directions are plotted in Figure 2g and h respectively. From Figure 2g, we found that the lamellar (100), (200), (300) diffraction peaks of PBDB-T are located at q_y of 0.293, 0.642, and 0.878 $Å^{-1}$ respectively; a result that is consistent with literature report [22]. The intensity of these peaks were largely unchanged upon thermal

annealing at 80 ºC, but increased significantly upon thermal annealing at 160 ºC. The (100) lamellar diffraction peak was also observed in the out-of-plane direction (see Fig. 2h). Although signals near q_z= 0.3 **Å**$^{-1}$ are blocked by the grid pattern of the 2D X-ray detector, a similar trend can be deduced that thermal annealing at 160 ºC increased the diffraction intensity significantly. This is evidence that the crystallinity of PBDB-T is enhanced after thermal annealing at 160 ºC. The Scherrer lengths for the in-plane D_{100} are calculated from the Scherrer equation and shown in Table 1, which continued to increase with higher annealing temperature. In the out-of-plane direction, a broad diffraction peak from 1.63 to 2.0 **Å**$^{-1}$ appeared upon annealing at 80 and 160 ºC, whilst this peak was absent in the as-cast film. Previous studies have suggested that this broad diffraction peak is associated with the convolution of (010) π-π stacking peaks of PBDB-T at q_z=1.74 Å^{-1} and IT-M at q_z=1.85 Å^{-1}. [22] We have deconvoluted the broad diffraction peak from 1.63 to 2.0 Å^{-1} via multi-peak fitting with Gaussian peaks (see Figure S2), and summarize the results in Table 1. When the thermal annealing temperature was 80 ºC, the intensity of the convoluted broad peak increased marginally and the (010) of PBDB-T and IT-M contributed *ca.* 60 and 40 % respectively to the total intensity of the peak. When the annealing temperature was enhanced to 160 ºC, the total intensity of this convoluted peak increased notably, and the contribution from PBDB-T accounted for *ca.* 68 % whilst that of IT-M only accounted for *ca.* 32%. This suggested that thermal annealing increases the π-π stacking of PBDB-T more effectively. The π–π stacking of macromolecules along the out-of-plane direction is known to provide a more ordered pathway for charge transport in the vertical direction of the photoactive layer towards electrodes, a characteristic that is desired for high performing solar cells[33]. This explains why a low-temperature annealing at 80 ºC can improve device efficiency, although it cannot increase the lamellar crystallinity.

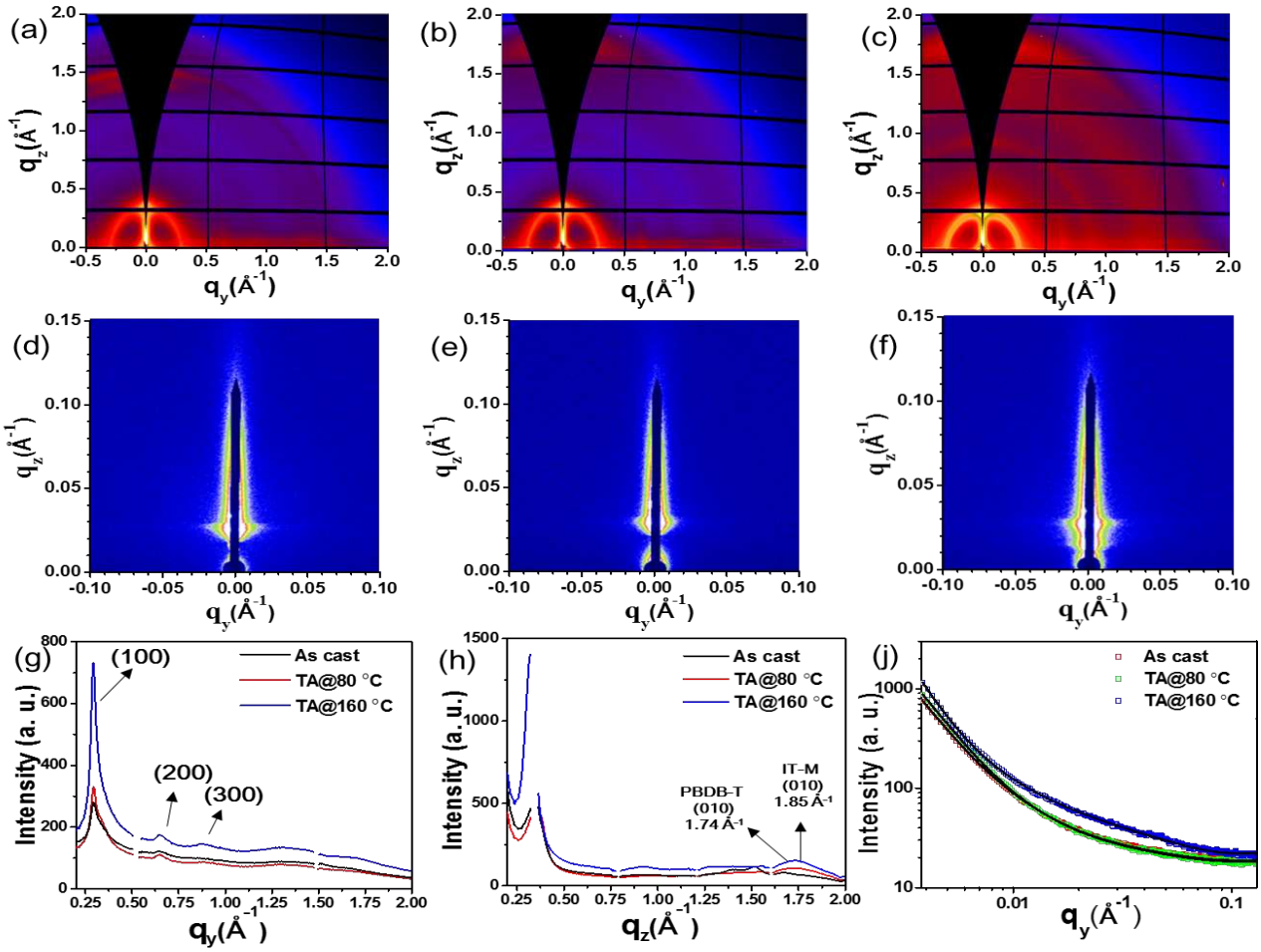

Figure 2 2D GIWAXS patterns of PBDB-T:IT-M films (a) as-cast, upon thermal annealing at (b) 80 °C and (c) 160 °C. 2D GISAXS patterns of PBDB-T:IT-M films (d) as-cast, upon thermal annealing at (e) 80 °C and (f) 160 °C. (g) In-plane GIWAXS profiles along q_y axis. (h) Out-of-plane GIWAXS profiles along q_z axis. (j) GISAXS profiles along q_y axis.

Table 1 Fitting parameters of 1D GISAXS profiles of PBDB-T:IT-M films with different thermal annealing treatments.

	PBDB-T D_{100} [nm]	PBDB-T D_{010} [nm]	PBDB-T D_{010} [%]	IT-M D_{010} [nm]	IT-M D_{010} [%]	ξ [nm]	η [nm]	D	$2R_g$ [nm]
As cast	11.8	-	-	-	-	46.9	16.5	2.01	57.3
TA@80 °C	12.2	8.3	60	8.6	40	45.7	21.3	1.93	71.6
TA@160 °C	13.5	8.6	68	8.1	32	98.0	22.4	1.65	66.3

In order to obtain more detailed information on the nanoscale phase separation in PBDB-T:IT-M films, GISAXS was employed to quantify the correlation length of each component in the active layer. 2D GISAXS patterns of PBDB-T:IT-M films with different annealing treatments are shown in Figure 2d-f, with the 1D profiles at the specular beam position within the region q_z=0.0038 to 0.02

Å^{-1} plotted in Figure 2h. It can be seen that the GISAXS images for all PBDB-T:IT-M films show a sharp decrease in intensity over the whole *q* region (< 0.02 Å^{-1}), without the appearance of any obvious shoulder in the middle-*q* region, a characteristic that is different from the fullerene-based photovoltaic blends where the aggregation of fullerene particles will lead to the appearance of a shoulder in the middle-*q* region. However, the diffraction intensity of PBDB-T:IT-M upon annealing at 160 °C increases in the middle-*q* region (see Fig. 2h); an observation that is similar to previous work[24,34]. The GISAXS intensities of these non-fullerene OPV films can be regarded as originating from X-ray scatter by IT-M clusters and PBDB-T polymer domains. The 1D GISAXS profiles were fitted using a universal model detailed in the supporting document using the fitting software SasView (Version 3.1.2). Table 1 shows the fitting parameters of our GISAXS profiles, where ξ is the correlation length of the PBDB-T phase, η and D are the correlation length and fractal dimension of IT-M aggregates, and 2Rg represents the size of clustered IT-M aggregates and is a product of η and D. Data fitting suggests that the PBDB-T correlation length of as casted film is 46.9 nm, and it barely changed after thermal annealing at 80 °C, but increased to 98.0 nm by annealing at 160 °C. Although larger polymer domains are beneficial for charge transport in the active layer, they also hamper efficient exciton dissociation[16], therefore both processes should be balanced appropriately. Interestingly, the increase in correlation length of IT-M clusters is less pronounced compared to PBDB-T, from *ca.* 16 nm in the as-cast film to 21-22 nm after thermal annealing. Notably, the fractal dimension of IT-M decreased from 2.01 to 1.93 upon annealing at 80 °C, and then to 1.65 upon annealing at 160 °C. This is an illustration that the aggregation of IT-M molecules changes from a compact state to a loose state; a consequence that will encourage interdiffusion between PBDB-T and IT-M molecules at their domain interfaces[35]. The difficulty by which PBDB-T and IT-M molecules undergo diffusion in the bulk prevents further propagation of this mixed region into PBDB-T and IT-M pure domains, therefore limiting its size. That is to say, the interface between PBDB-T and IT-M evolves from a relatively sharp interface in the as-cast film to a diffuse interface upon high temperature annealing at 160 °C (see Figure 3c), with the interfaces obtained upon annealing at 80 °C still retaining a similar character to those in the as-cast film as there is no significant change of its fractional dimensionality (see Table 1). The impact of this diffused interface to the photovoltaic properties will be discussed in a later section.

We proceeded to determine the vertical component distributions in PBDB-T:IT-M films using X-ray photoelectron spectroscopy (XPS) with a gas-cluster etching accessory. PBDB-T:IT-M blend

films were cast on PEDOT:PSS and TiO_2 surfaces to explore the annealing effects on vertical stratification. To identify PBDB-T and IT-M, we first measured the PBDB-T and IT-M pure films to identify the C, N, O, and S elemental content of PBDB-T and IT-M. We then used the ratio of N/S, C/S and C/O to detect the PBDB-T and IT-M content and use the percentage of S to compare the ratio of PBDB-T and IT-M. The thickness of PBDB-T:IT-M films were all around 120 nm. The normalized depth profiles are shown in Figure 3a and b for films cast on TiO_2 and PEDOT:PSS respectively. For the normalization, we have defined the air interface as thickness 0, and the substrate interface as thickness 1 where the TiO_2 and PEDOT:PSS signal starts to appear and their intensity increases sharply as the etch penetrates further into the substrate[36]. As shown in Figure 3a and b, PBDB-T:IT-M films cast on both substrates contain a PBDB-T-rich surface layer. The content of the PBDB-T component in the surface layer is approximately 70 % as a PBDB-T/IT-M ratio of 2.5-3 has been determined. From the second testing point after running the XPS etching, the PBDB-T content has reduced significantly, the ratio of PBDB-T/IT-M from the second or third test started to reach the plateau value of 1 which is the ratio in the bulk of the blend film. We can therefore approximately determine that the PBDB-T-rich surface layer has a thickness around 6 nm, although this value can be obtained with more confidence if the step size of our XPS etching can be reduced further. The ratio of PBDB-T/IT-M reduces as the XPS probed deeper into the film, reaching a plateau value of 1 in the bulk of the blend film. This is a result of the lower surface free energy of PBDB-T, with a value of 20.2 mN/m compared to ca. 28 mN/m of TiO_2, which causes it to migrate upwards and locate at the surface region of the blend film to minimize the total surface free energy of the system.[13,37] After thermal annealing at 80 ^oC, the depth profiles were largely unchanged, suggesting that there is not enough diffusion of PBDB-T and IT-M at this low temperature to influence vertical component distribution. Upon thermal annealing at a relatively high temperature of 160 ^oC, the PBDB-T:IT-M film cast on TiO_2 substrate retained the same character of vertical component distribution (see Figure 3a). Notably, the ratio of PBDB-T/IT-M in the surface region of the film cast on PEDOT:PSS and thermally annealed at 160 ^oC reduced from the original value over 2.5 to around 1 and remained rather constant throughout the bulk of the film, suggesting that the vertical non-uniform component distribution is now absent. The two substrates employed in this work therefore lead to two different vertical component distributions in PBDB-T:IT-M blend films after thermal annealing at a relatively high temperature of 160 ^oC. These substrate-directed depth profiles have been widely observed in the literature in many fullerene-based OPV blend systems[38,39].

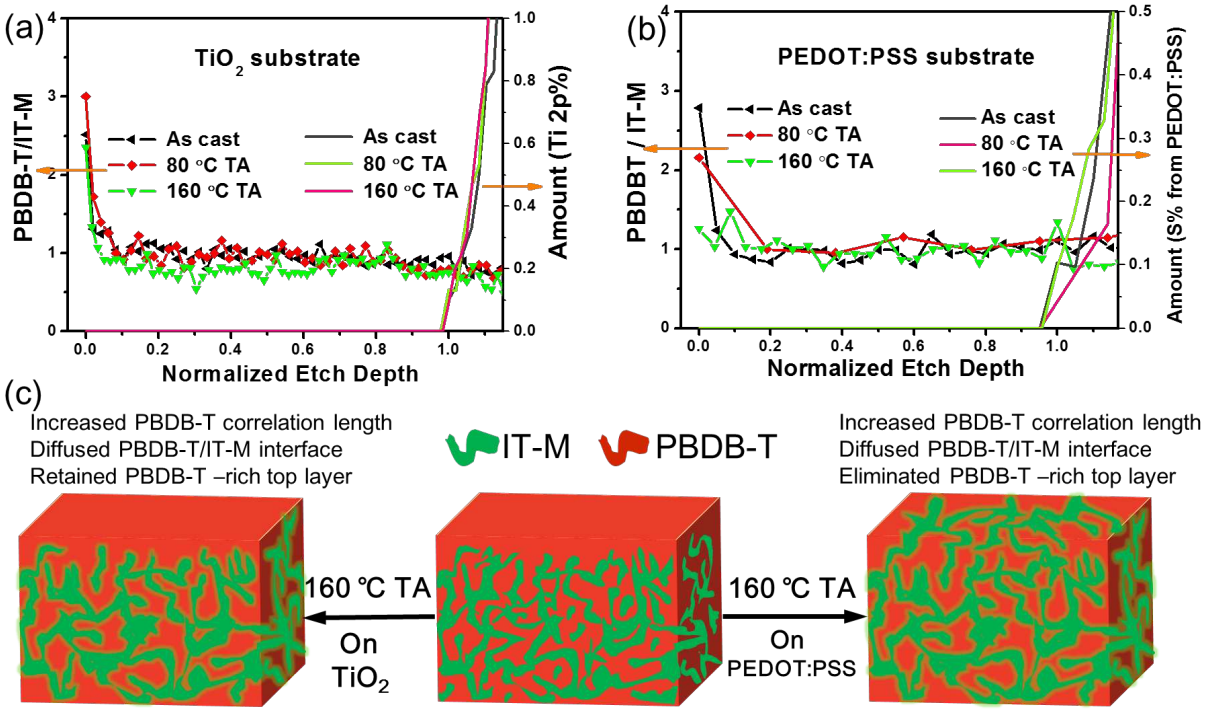

Figure 3 XPS Depth profiles of PBDB-T:IT-M films casting on (a) TiO_2 and (b) PEODT:PSS substrates at different annealing temperature. (c) Schematic of three-dimensional morphology evolution upon thermal annealing at 160 °C on TiO_2 and (b) PEODT:PSS substrates.

In order to confirm the validity of the XPS measurements, we have measured the surface free energies of PBDB-T:IT-M blend films after different annealing treatments, as an indirect approach to determine which materials are located at the film surface. As mentioned earlier, PBDB-T and IT-M have different surface free energies of *ca.* 20.2 and 28 mN/m respectively, cast on either PEDOT:PSS or TiO_2. These values do not change much after thermal annealing at either 80 or 160 °C, indicating that changes in the molecular ordering of the materials will not influence their surface free energy. Therefore any surface energy changes of a blend film can be regarded as component changes at the film surface. The surface energy of as-cast the PBDB-T:IT-M blend film, on either TiO_2 or PEDOT:PSS surfaces, is around 20.5 mN/m, a value that is close to that of PBDB-T and therefore supports our earlier conclusion that a PBDB-T-rich layer is located at the film surface. These surface energy values did not change upon annealing at 80 °C, suggesting minimal component changes at the film surface. This is also observed for PBDB-T:IT-M blend film cast on TiO_2 and thermally annealed at 160 °C, however, the surface free energy increased to 22.8 mN/m when the film was cast on PEDOT:PSS, a phenomenon that indicates the increased content of IT-M at the surface region. The surface energy measurements here therefore fully support our XPS observations on the vertical

component distributions in PBDB-T:IT-M blend films.

Table 2 Surface energies of PBDB-T, IT-M and PBDB-T:IT-M films on PEDOT:PSS and TiO_2 substrates.

	PBDB-T on PEDOT:PSS (mN/m)	PBDB-T on TiO_2 (mN/m)	IT-M on PEDOT:PSS (mN/m)	IT-M on TiO_2 (mN/m)	PBDB-T:IT-M on PEDOT:PSS (mN/m)	PBDB-T:IT-M on TiO_2 (mN/m)
As cast	20.1	20.0	27.9	28.2	20.4	20.5
TA@80 °C	20.2	20.3	28.3	28.3	20.5	20.4
TA@160 °C	20.2	20.2	28.1	28.2	22.8	20.3

Based on the average morphological characteristics in the lateral direction probed via GI-WAXS and GI-SAXS measurements, and vertical component distributions revealed by XPS and surface energy analysis, we have summarized the three-dimensional morphology characteristics of PBDB-T:IT-M blend films in Figure 3c. Thermal annealing at a low temperature of 80 °C increases stacking order in the blend films, without any notable impact on the crystallinity and vertical component redistribution. Thermal annealing at a relatively high temperature of 160 °C increased the average correlation length of PBDB-T and leads to the formation of a diffused interface with IT-M. After annealing at 160 °C, the PBDB-T-rich surface layer remains in an PBDB-T:IT-M blend film cast on TiO_2 substrate, but is absent in a blend film cast on PEDOT:PSS substrate. We tentatively attribute this contrasting effect as a result of attractive interactions between macromolecules PBDB-T and PEDOT:PSS under high annealing temperature, whilst this interaction is absent at the interface of active layer and inorganic TiO_2 nanoparticles. This mutual attraction between PEDOT:PSS and PBDB-T can restrain the segregation of PBDB-T towards the film surface due to its lower surface free energy[40], and therefore create a uniform distribution of PBDB-T in the vertical direction of the PBDB-T:IT-M blend film.

To assess the three-dimensional morphology of the active layer on device performance, we have studied the photovoltaic properties of PBDB-T:IT-M solar cells in both conventional and inverted configurations upon different annealing treatments. The J-V characteristics and EQE of these devices are plotted in Figure 4 and Table 3. The calculated J_{sc} from EQE spectra are *ca.* 5% less that the J_{sc} values obtained from J-V scans, and therefore confirms the validity of our J-V measurements. It is apparent that the PCEs of our inverted devices are generally higher than those of conventional devices upon the same post-treatment, a result that confirms the benefit of fabricating OPV devices

according to this architecture. As discussed above, there exists a PBDB-T-rich phase at the top surface region of the photoactive layer near the anode in inverted devices, which can facilitate hole transport from the active layer to the hole transport layer (HTL) while blocking electrons that transport towards the HTL. The optimum annealing temperature has been found to be 80 °C for the inverted devices, due to increased π-π stacking by this treatment. Although the crystallinity of PBDB-T was increased upon thermal annealing at 160 °C, its correlation length was almost doubled and a diffuse interface with IT-M was formed; characteristics that may perturb the exciton diffusion and dissociation processes and therefore reduced the short-circuit current (see Table 3). In conventional devices, a PBDB-T-rich layer near the cathode in the as-cast and 80 °C-annealed PBDB-T:IT-M films will in principle hinder electron transport towards the cathode, therefore leading to generally lower J_{sc} and PCE values. However, this PBDB-T-rich layer is absent upon thermal annealing at 160 °C; a change that will facilitate electron transport towards to cathode and compensate for unfavorable optoelectronic property changes caused by this high temperature annealing. Therefore the optimum annealing temperature is 160 °C in conventional devices.

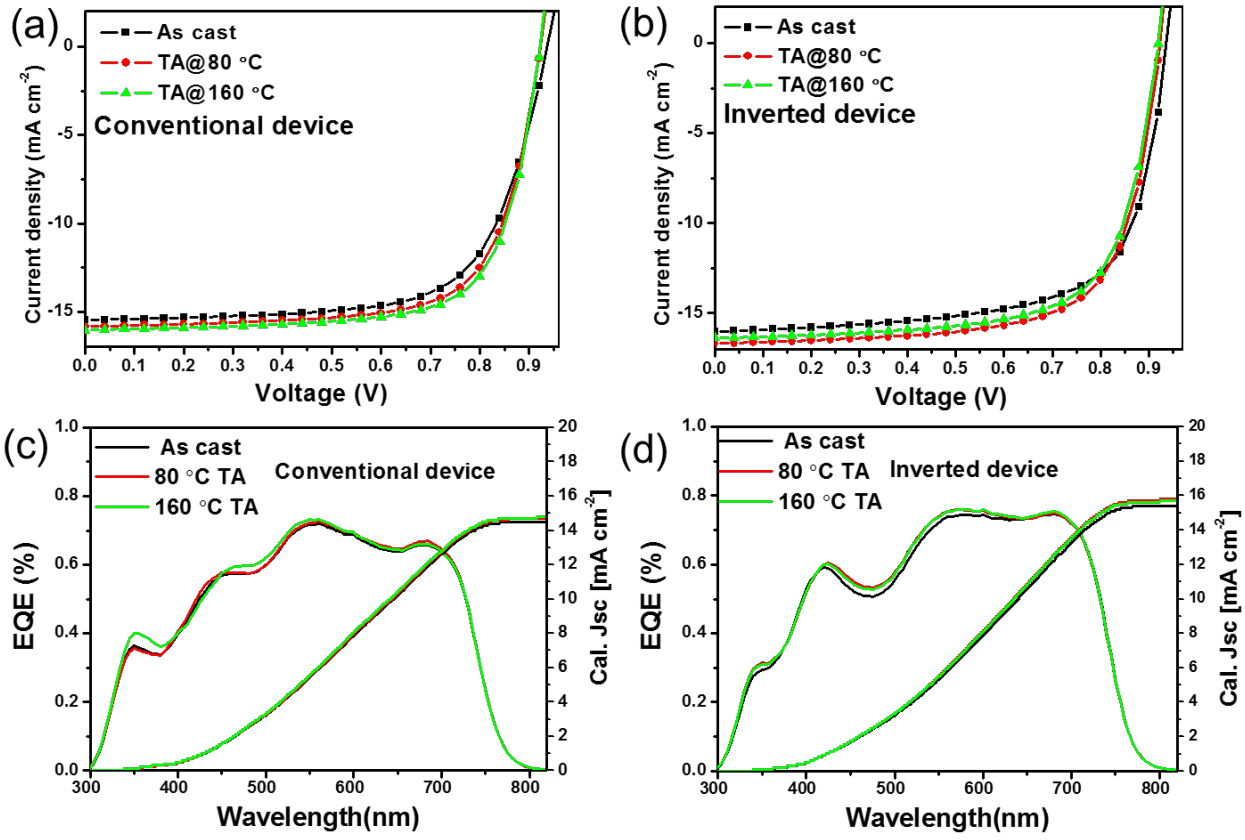

Figure 4 Champion J-V curves of (a) conventional and (b) inverted PBDB-T:IT-M OPVs upon annealing at different temperatures. EQE spectra of (c) conventional and (d) inverted OPVs.

Table 3 Summary of photovoltaic parameters of conventional and inverted PBDB-T:IT-M OPVs measured at an illumination of AM 1.5G at 100 mW cm^{-2}. The statistical data presented were obtained from over 15 individual devices.

PBDB-T:IT-M	FF [%]	Jsc [mA cm^{-2}]	Voc [V]	Avg. PCE [%]	Max. PCE [%]
As cast (Conventional)	68.5±0.61	15.3±0.28	0.936±0.01	9.7 ±0.16	9.9
80 °C TA (Conventional)	70.5±0.92	15.6±0.52	0.924±0.01	10.2±0.21	10.4
160 °C TA (Conventional)	70.8±0.31	15.8±0.21	0.923±0.01	10.4±0.15	10.6
As cast (Inverted)	68.2±0.94	16.1±0.80	0.936±0.01	10.3±0.32	10.4
80 °C TA (Inverted)	70.1±0.73	16.7±0.41	0.923±0.01	10.8±0.28	11.2
160 °C TA (Inverted)	69.5±0.81	16.4±0.57	0.920±0.01	10.5±0.43	10.7

To evaluate exciton dissociation and charge collection processes in our PBDB-T:IT-M OPV devices, we have studied the photo current density (J_{ph}) as a function of the effective voltage (V_{eff}) of devices after different annealing treatments. Here, J_{ph} is defined as $J_{ph} = J_{light} - J_{dark}$, where J_{light} and J_{dark} are the photocurrent densities under illumination and dark respectively, and V_{eff} is defined as $V_{eff} = V_0 - V_a$, where V_0 is the voltage when $J_{ph} = 0$ and V_a is the applied voltage. As shown in Figure 5a and d, the J_{ph} of all devices saturates at large V_{eff}, suggesting that all photogenerated excitons have been dissociated into free carriers and all carriers are collected by the electrodes without any charge recombination[41]. The saturated short-circuit current density (J_{sat}) of all devices are roughly constant at 16.5 mA cm^{-2}; a result that is consistent with the similar absorption ability of these PBDB-T:IT-M films (see Figure S3). The J_{ph}/J_{sat} value under short-circuit conditions represents the exciton dissociation efficiency (P_{diss}), whilst the J_{ph}/J_{sat} value under the maximal power output condition represents the charge transport and collection efficiency (P_{coll})[42]. As shown in Table 4, both in conventional and inverted devices, devices that are annealed at 80 °C display the optimum exciton dissociation efficiency, as the maximum P_{diss} was found at this annealing temperature. In addition, the P_{coll} values of all inverted devices are generally higher than those of conventional devices, with the correct vertical component distributions in inverted devices contributing at least partly to this favorable effect.

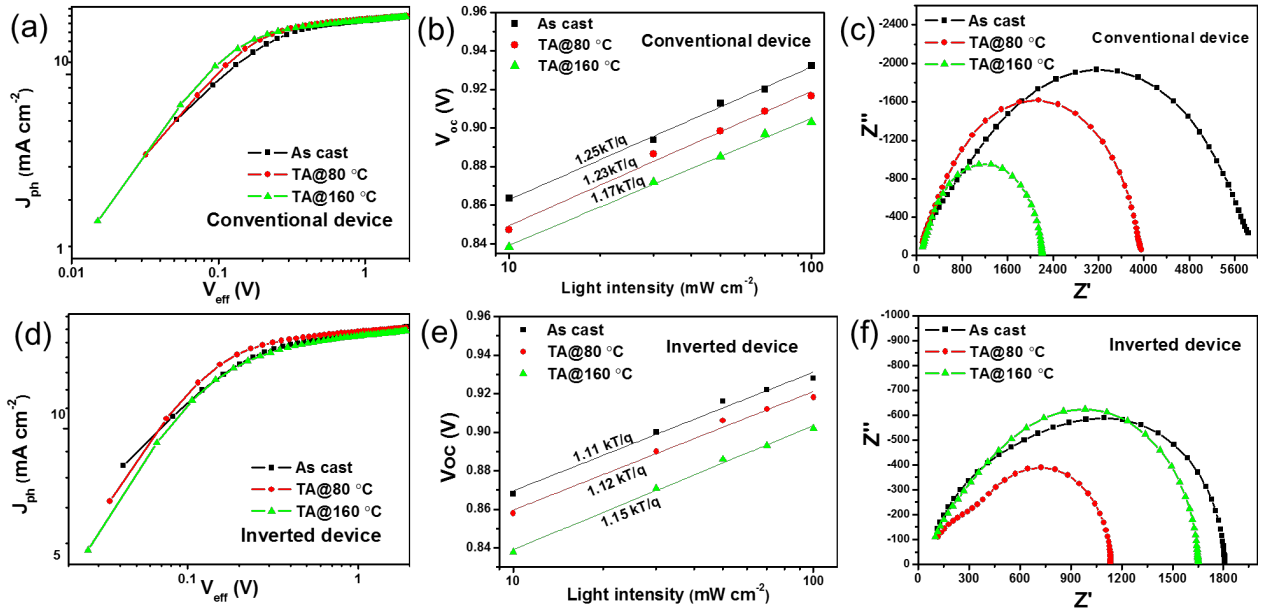

Figure 5 Photocurrent density versus effective voltage curves of (a) conventional and (d) inverted PBDB-T:IT-M OPVs upon annealing at different temperatures. V_{OC} versus light intensity with the slope gradient indicated in brackets of (b) conventional and (e) inverted PBDB-T:IT-M OPVs. Nyquist plots of impedance spectra of (c) conventional and (f) inverted PBDB-T:IT-M OPVs measured with an applied bias of V_{OC} under 0.1 sun irradiation.

Table 4 J_{sat}, P_{diss} and P_{coll} of PBDB-T:IT-M OPVs with different annealing treatments.

	J_{sat} [mA cm^{-2}]	P_{diss} [%]	P_{coll} [%]
As cast (Conventional)	16.4	95.9	78.4
TA@80 °C (Conventional)	16.4	96.7	80.2
TA@160 °C (Conventional)	16.5	96.0	81.5
As cast (Inverted)	16.6	96.0	82.3
TA@80 °C (Inverted)	16.8	98.0	87.1
TA@160 °C (Inverted)	16.8	96.8	82.1

Table 5 Electron and hole mobilities of PBDB-T:IT-M OPVs after different annealing treatments.

	Electron mobility (μ_e) cm^{2}V^{-1}S^{-1}	Hole mobility (μ_h) cm^{2}V^{-1}S^{-1}	μ_e/μ_h
As cast	3.3 x10^{-4}	1.4 x10^{-4}	2.35
TA@80 °C	5.5 x10^{-4}	3.3 x10^{-4}	1.66
TA@160 °C	8.8 x10^{-4}	4.1x 10^{-4}	2.15

Table 6 Summary of fitting parameters of PBDB-T:IT-M OPVs from Nyquist plots.

	R_1 [Ω]	R_2 [Ω]	CPE-T2 [F]	CPE-P2	R_3 [Ω]	CPE-T3 [F]	CPE-P3
As cast (Conventional)	71	440	5.5 E-8	0.828	1925	4.6 E-9	0.982
TA@80 °C (Conventional)	74	337	3.2 E-8	0.855	1446	5.9 E-9	0.981
TA@160 °C (Conventional)	69	362	1.8 E-8	0.858	1221	6.9 E-9	0.970
As cast (Inverted)	64	377	2.9 E-8	0.835	1223	9.7 E-9	0.951
TA@80 °C (Inverted)	61	313	1.1 E-8	0.865	763	1.4 E-8	0.962
TA@160 °C (Inverted)	63	372	7.3 E-9	0.876	983	1.5E-8	0.946

The hole (μ_h) and electron (μ_e) mobilities were extracted from dark J-V curves of hole-only and electron-only devices to investigate their charge transfer characteristics. As shown in Figure S4, and Table 5, thermal annealing at both temperatures increased both μ_h and μ_e. We also found that the ratios of μ_e/μ_h are 2.35, 1.66 and 2.15 for the as-cast devices, and those upon annealing at 80 and 160 °C, respectively. Annealing at 80 °C therefore provided the most balanced carrier mobility. The imbalanced μ_e/μ_h ratio of devices upon annealing at 160 °C may result in more recombination losses in solar cells[43]. To gain more insight into charge recombination process in the OPVs, we evaluated the light intensity dependent V_{oc}. In this analysis, a unity slope (units of kT/q) is a signature of bimolecular recombination in the device, whilst a slope greater than unity indicates that both bimolecular and trap-assisted recombination operate in the device[44]. As shown in Figure 5b and e, slopes of all inverted devices are *ca.* 1.1 kT/q upon different annealing treatments, suggesting that bimolecular recombination dominates but trap-assisted recombination also operates. However, in conventional devices (especially in the as-cast device and the device that was thermally annealing at 80 °C in which an "unfavourable" layer of PBDB-T is located near the cathode interface) the slope is higher than 1.2 kT/q, suggesting an increased amount of trap-assisted recombination in these devices. This slope was then effectively reduced to 1.17 kT/q once this "unfavourable" layer was removed by annealing at a high temperature of 160 °C.

Alternating current impedance spectroscopy (IS) was also performed to gain in-depth understanding of the charge transport and recombination processes. Figure 5c and f shows the corresponding Nyquist plots of the conventional and inverted devices after different annealing treatments, measured under a small voltage perturbation with an applied bias near open circuit voltage and under 0.1 sun irradiation. As the Nyquist plots of all devices all obey a double semi-circle law, we have employed an equivalent circuit model (see Figure S5) with two resistances

(R_2 and R_3) and constant phase elements (CPE_2 and CPE_3) in parallel to fit the curves[45,46]. R_1 corresponds to the series resistance of the device, which remains almost constant in all devices. R_2 and CPE_2 correspond to the resistance and capacitance of the active layer, which signifies charge transport at the PBDB-T/IT-M interface. It can be seen that annealing at 80 °C leads to the lowest values of R_2 in both conventional and inverted devices, indicating that this low temperature annealing can provide a good pathway for charge transport in the active layer. A lower CPE-T2 implies a reduced interfacial area between electron donors and acceptors[47,48], with this result being consistent with our morphology characterization of increased correlation lengths of PBDB-T and IT-M after thermal annealing. As described in previous work, R_3 and CPE_3 are associated with two electrical contacts between the active layer and electrodes[49]. Here, a higher R_3 suggests that the interface between the active layer and electrodes is detrimental for charge transport at the electrode interfaces, whilst a higher CPE-T3 suggests there exist more pathways for charge transport. The R_3 values for conventional devices are generally higher than those of inverted devices, with conventional devices annealed at 160 °C having a reduced value of R_3 due to the optimum vertical component distribution facilitating charge transport. The CPE-T3 of all devices increased with the increasing annealing temperature, correlating with the improved charge transport.

3. Conclusion

In summary, we have investigated the morphological characteristics of PBDB-T:IT-M photovoltaic blends in both lateral and vertical directions, and have correlated the three-dimensional morphology with photovoltaic properties in both conventional and inverted solar cell devices. We found that low temperature annealing at 80 °C increases the stacking order of the blends without affecting the overall crystallinity and vertical component distributions. Although thermal annealing at a high temperature of 160 °C can improve the crystallinity of PBDB-T:IT-M films and increase charge mobility, this high-temperature treatment doubles the correlation length of PBDB-T and leads to the formation of a diffuse interface between PBDB-T and IT-M domains, a characteristic that, from our device studies, proved to be detrimental to photovoltaic performance. A PBDB-T-rich surface layer was identified in PBDB-T:IT-M blend films cast on both TiO_2 and PEDOT:PSS substrates. This PBDB-T-rich surface layer remained in inverted devices but was removed from conventional devices upon annealing at 160 °C, therefore creating a “correct” component distribution near the electrode interface in both conventional and inverted devices. The comprehensive

understanding of morphology in three-dimensions explains the contrasting optimum annealing temperature of 80 and 160 °C respectively found in inverted and conventional PBDB-T:IT-M devices. Overall, our work suggests that the characterization of nanoscale morphology in three dimensions is necessary to fully understand the photovoltaic performance in conventional and inverted non-fullerene organic solar cells.

4. Experimental Section

4.1. Materials

PBDB-T and IT-M were purchased from Solarmer Materials (Beijing) Inc. TiO_2 nanoparticles were synthesized according to our previous report[50]. The TiO_2 nanoparticles were blended with a titanium oxide bis(2,4-pentanedionate) (TOPD) additive which acts as a binder to reduce morphological defects between TiO_2 nanoparticles, and reduced its work function from -4.43 eV to -4.23 eV. The TiO_2 composite films received UV light treatments and further rinsing with the ethanolamine (EA) to obtain a further reduced work function of -4.14 eV, and has been demonstrated as an efficient ETL layer to prepare high performance inverted polymer solar cells. PEDOT:PSS (Clevios AI 4083) was purchased from Heraeus, Germany. Unless otherwise stated, all chemicals and solvents were of reagent grade and used as received.

4.2. Fabrication of solar cells

Solar cells were fabricated with both conventional and inverted structures. The prepatterned ITO-glass substrates (resistance ca. 15 Ω per square) were cleaned by sequential sonication in water, ethanol, and isopropyl alcohol for 10 minutes each, before drying at 100°C on a hotplate. These substrates were further treated with u ltraviolet/ozone for 10 min before solution processing. For the fabrication of conventional devices, 40 nm thick PEDOT:PSS films were spin-coated onto cleaned ITO substrates, then dried at 150 °C for 10 min in air. The active layer was then deposited on top of the PEDOT:PSS layer by spin-coating in a nitrogen-filled glovebox from a 14 mg/ml chlorobenzene solution (with 1 vol.% DIO) of PBDB-T:IT-M (weight ratio of PBDB-T:IT-M fixed at 1:1) to obtain films of 100 nm thickness. For conventional devices without annealing, 5 nm Ca and 100 nm Ag were thermally evaporated onto the as-cast film directly under high vacuum, forming the cathode. For the device with 80 °C and 160 °C thermal treatments, as-cast films were heated on a hotplate at 80 and 160 °C in a nitrogen environment for 30 min before evaporating the Ca and Ag layers. For the

fabrication of inverted devices, 20 nm-thick TiO_2 composite films were cast from a TiO_2 blend dispersion by spin-coating at 3000 rpm, followed by thermal annealing at 150 ^oC for 30 min. The films were then transferred into an N_2-filled glove box and irradiated 10 min under a 254 nm UV light before rinsing with the ethanolamine (EA) solution (1 wt. % in 2-methoxyethanol) at 3000 rpm. The casting and the annealing procedure of photoactive layer on TiO_2 films are the same as described above. Following this, 10 nm MoO_3 and 100 nm Ag were thermally evaporated to form an anode under high vacuum.

4.3. Characterization

Film absorption spectra were measured using a UV-Visible spectrophotometer (HITACHI, Japan). Film thickness was measured using a spectroscopic ellipsometer (J. A. Woollam, USA). Water contact angle measurements were performed using a water contact angle measurement system (Attension Theta Lite, Sweden), and the surface energy was calculated using the equation of state. XPS data were obtained using a Kratos Axis Supra (Kratos Analytical, Manchester, UK) using a monochromated Al Kα source. All spectra were recorded using a charge neutralizer to limit differential charging. The main carbon peak is charge referenced to 284.5 eV.[51,52] The method of XPS for depth profiles and calculating component is shown in supporting information. GISAXS measurements were conducted using the beamline BL16B1 at the Shanghai Synchrotron Radiation Facility in China. GIWAXS measurements were conducted at beamline I07 at Diamond Light Source in the U.K. The energy of the X-ray beam was 10 keV with measured data obtained at the sample critical angle (~0.2˚). Films were prepared on Si substrates. Data obtained was calibrated using silver behenate powder and analysed using the DAWN software package (http://dawnsci.org). Duplicate tests were conducted for GIWAXS, GISAXS and XPS measurements to make sure the reported results are representative.

Device J-V characterization was performed under AM 1.5G (100 mW cm^{-2}) using a Newport 3A solar simulator (Newport, USA) in air at room temperature. The light intensity was calibrated using a standard silicon reference cell certified by the National Renewable Energy Laboratory (NREL, USA). J-V characteristics were recorded using J-V sweep software developed by Ossila Ltd. (UK) and a Keithley 2612B (USA) source meter unit. An aperture mask was placed over the devices to accurately define a testing area of 2.12 mm^2 on each pixel and to eliminate the influence of stray and wave guided light. External quantum efficiency (EQE) was measured with a Zolix (China) EQE

system equipped with a standard Si diode. Impedance measurements were performed on an XM-studio electrochemical workstation (Solartron, U.K.). EIS measurements were performed under a small voltage perturbation with an applied bias near open circuit voltage and under 0.1 sun irradiation. Equivalent circuit simulations were conducted using the software package ZView 3.1 (Scribner Associate, Inc., USA).

Acknowledgments

This work was supported by the National Natural Science Foundation of China (Grants No. 21774097, 21504065), the Natural Science Foundation of Hubei Province (2018CFA055), and the Fundamental Research Funds for the Central Universities (WUT: 2017-YB-010) of China. A.J.P. thanks the Engineering and Physical Sciences Research Council (EPSRC) for support (EP/M024873/1, Singlet Fission Photon Multipliers - Adding Efficiency to Silicon Solar Cells). D.G.L. thanks the EPSRC for support through research grant EP/M025020/1 'High resolution mapping of performance and degradation mechanisms in printable photovoltaic devices'. We thank the beamline BL16B1 at Shanghai Synchrotron Radiation Facility (China) for providing the beam time and help during experiments, and thank Diamond Light Source for access to beamline I07 (SI17223-1) that contributed to the GIWAXS results. We thank Edoardo Ruggeri (University of Cambridge) for help with the GIWAXS measurements and also thank Dr. Zhihong Chen (Department of Physics, Wuhan University of Technology) for helping with the GISAXS data analysis.

References

1 P. Chen, G. Li, X. Zhan, Y. Yang, *Nat. Photonics* **2018**, 12, 131.

2 J. Hou, O. Inganas, R. H. Friend, F. Gao, *Nat. Mater.* **2018**, 17, 2018, 17, 119.

3 S. Holliday, R. S. Ashraf, A. Wadsworth, D. Baran, S. A. Yousaf, C. B. Nielsen, C. H. Tan, S. D. Dimitrov, Z. Shang, N. Gasparini, M. Alamoudi, F. Laquai, C. J. Brabec, A. Salleo, J. R. Durrent, I. McCulloch, *Nat. Mater.* **2016**, 7, 11585.

4 C. Yan, S. Barlow, Z. Wang, H. Yan, A. K. Y. Jen, S. R. Marder, X. Zhan, *Nat. Rev. Mat.* **2018**, 3, 18003.

5 W. Zhao, S. Li, H. Yao, S. Zhang, Y. Zhang, B. Yang, J. Hou, *J. Am. Chem. Soc.* **2017**, 139, 7148.

6 Z. Xiao, L. Ding, J. Wang, *Sci. Bull.* **2017**, 62, 1562-1564.

7 H. Li, Z. Xiao, L. Ding, J. Wang, *Sci. Bull.* **2018**, 63, 340.

8 Y. Cui, H. Yao, C. Yang, S. Zhang, J. Hou, *ACTA POLYMEICA SINICA* **2018**, 2, 223.

9 G. G. Belmonte, P. P. Boix, J. Bisquart, M. Lenes, H. J. Bolink, A. L. Rosa, S. Filippone, N.

Martin, *J. Phys. Chem. Lett.* **2010**, 1, 2566-2571.

10 L. Ye, H. Hu, M. Ghasemi, T. Wang, B. A. Collins, J. H. Kim, K. Jiang, J. H. Carpenter, H. Li, Z. Li, T. McAfee, J. Zhao, X. Chen, J. L. Y. Lai, T. Ma, J. L. Bredas, H. Yan, H. Ade, *Nat. Mater.* **2018**, 17, 253.

11 Q. Fan, Y. Wan, M. Zhang, B. Wu, X. Guo, Y. Jiang, W. Li, B. Guo, C. Ye, W. Su, J. Fang, X. Ou, F. Liu, Z. Wei, T. C. Sum, T. R. Russell, Y. Li, *Adv. Mater.* **2018**, 30, 1704546.

12 Y. Lin, F. Zhao, Y. Wu, K. Chen, Y. Xia, G. Li, S. K. K. Prasad, J. Zhu, L. Huo, H. Bin, Z. G. Zhang, X. Guo, M. Zhang, Y. Sun, F. Gao, Z. Wei, W. Ma, C. Wang, J. Hodgkiss, Z. Bo, O. Inganäs, Y. Li, X. Zhan, *Adv. Mater.* **2017**, 29, 1604155.

13 Y. Yan, X. Liu, T. Wang, *Adv. Mater.* **2017**, 1601674.

14 P. M. Buschbaum, *Adv. Mater.* **2014**, 7692.

15 T. Wang, A. D. F. Dunbar, P. A. Staniec, A. J. Pearson, P. E. Hopkison, J. E. Macdonald, S. Lilliu, C. Pizzey, N. J. Terrill, A. M. Donald, A. J. Ryan, R. A. L. Jones, D. G. Lidzey, *Soft Matter* **2010**, 6, 4128.

16 Y. Huang, E. J. Kramer, A. J. Heeger, G. C. Bazan, *Chem. Rev.* **2014**, 114, 7006.

17 T. Wang, N. W. Scarratt, H. Yi, D. F. Dunbar,A. J. Pearson, D. C. Watters, T. S. Glen, A. C. Brook, J. Kingsley, A. R. Buckley, M. W. A. Skoda, A. M. Donald, R. A. L. Jones, A. Iraqi, D. G. Lidzey, *Adv. Energy Mater.* **2013**, 3, 505.

18 J. Huang, J. H. Carpenter, C. Z. Li, J. S. Yu, H. Ade, A. K. Y. Jen, *Adv. Mater.* **2016**, 28, 967-974

19 M. C. Quiles, T. Ferenczi, T. Agostinelli, P. G. Etchegoin, Y. Kim, T. Anthopoulous, P. N. Stavrinou, D. D. C. Bradley, J. Nelson, *Nat. Mater.* **2008**, 7, 158.

20 W. Li, Y. Yan, Y. Gong, J. Cai, F. Cai, R. S. Guiney, D. Liu, A. J. Pearson, D. G. Lidzey, T. Wang, *Adv. Funct. Mater.* **2018**, 28, 1704212.

21 H. Cheun, J. D. Berrigan, Y. Zhou, M. Fenoll, J. Shim, C. Fuentes-Hernandez, K. H. Sandhageb, B. Kippelen, *Energy Environ. Sci.* **2011**, 4, 3456.

22 S. Li, L. Ye, W. Zhao, S. Zhang, S. Mukherjee, H. Ade, J. Hou, *Adv. Mater.* **2016**, 28, 9423.

23 X. Liu, L. Ye, W. Zhao, S. Zhang, S. Li, G. M. Su, C. Wang, H. Ade, J. Hou, Mater. *Chem. Front.* **2017**, 1, 2057.

24 L. Ye, W. Zhao, S. Li, S. Mukherjee, J. H. Carpenter, O. Awartani, X. Jiao, J. Hou, H. Ade, *Adv. Energy Mater.* **2016**, 1602000.

25 L. Ye, B. A. Collins, X. Jiao, J. Zhao, H. Yan, H. Ade, *Adv. Energy Mater.* **2018**, 1703058.

26 T Wang, N. W. Scarratt, H. Yi, I. F. Coleman, Y. Zhang, R. T. Grant, J. Yao, M. W. A. Skoda, A. D. F. Dunbar, R. A. L. Jones, A. Iraqi, D. G. Lidzey, *J. Mater. Chem. C* **2015**, 3, 4007.

27 M. Kim, J. H. Kim, H. H. Choi, J. H. Park, S. B. Jo, M. Sim, J. S. Kim, H. Jinnai, Y. D. Park, K.

Cho, *Adv. Energy Mater.* **2014**, 4, 1300612.

28 Y. Vaynzof, T. J. K, Brenner, D. Kabra, H. Sirringhaus, R. H. Friend, *Adv. Funct. Mater.* **2012**, 22, 2418.

29 B. J. Moon, G. Y. Lee, M. J. Im, S. Song, T. Park, *Nanoscale* **2014**, 6, 2440.

30 M. B. Upama, N. K. Elumalai, M. A. Mahmud, M. Wright, D. Wang, C. Xu, A. Uddin, *Sol. Energy Mat. Sol. C*. **2018**, 176, 109.

31 T. Wang, A. J. Pearson, A. D. F. Dunbar, P. A. Staniec, D. C. Watters, H. Yi, A. J. Ryan, R. A. L. Jones, A. Iraqi, D. G. Lidzey, *Adv. Funct. Mater.* **2012**, 22, 1399.

32 X. Ouyang, R. Peng, L. Ai, X. Zhang, Z. Ge, *Nat. Photonics* **2015**, 9, 520

33 A. T. Yiu, P. M. Beaujuge, O. P. Lee, C. H. Woo, M. F. Toney, J. M. J. Fréchet, *J. Am. Chem. Soc.* **2012**, 134, 2180.

34 H. C. Liao, C. S. Tsao, Y. T. Shao, S. Y. Chang, Y. C. Huang, C. M. Chuamg, T. H. Lin, C. Y. Chen, C. J. Su, U. S. Jeng, Y. F. Chen, W. F. Su, *Energy Environ. Sci.* **2013**, 6, 1938-1948.

35 J. Mai, T. Lau, J. Li, S. H. Peng, C. S. Hsu, U. S. Jeng, J. Zeng, N. Zhao, X. Xiao, X. Lu, *Chem. Mater.* **2016**, 28, 6186.

36 W. Song, X. Fan, B. Xu, F. Yan, H. Cui, Q. Wei, R. Peng, L. Hong, J. Huang, Z. Ge, *Adv. Mater.* **2018**, 1800075

37 L. Huang, G. Wang, W. Zhou, B. Fu, X. Cheng, L. Zhang, Z. Yuan, S. Xiong, L. Zhang, Y. Xie, A. Zhang, Y. Zhang, W. Ma, W. Li, Y. Zhou, E. Reichmanis, Y. Chen, *ACS Nano* **2018**, 12, 4440.

38 R. Hansson, L. K. Ericsson, N. P. Holmes, J. Rysz, A. Opitz, M. C. Quiles, E. Wang, M. G. Barr, A. L. D. Kilcoyne, P. Dastoor, E. Moons, *J. Mater. Chem. A* **2015**, 3, 6970-6979

39 Y. Wang, H. Zhu, Z. Shi, F. Wang, B. Zhang, S. Dai, Z. Tan, *J. Mater. Chem. A* **2017**, 5, 2319-2327

40 M. A. Ruderer, P. Müller-Buschbaum, *Soft Matter*, **2011**, 7, 5482.

41 P. G. Karagiannidis, D. Georgiou, C. Pitsalidis, A. Laskarakis, S. Logothetidis, *Mater. Chem. Phys.* **2011**, 129, 1207.

42 Z. He, C. Zhong, X. Huang, W. Y. Wong, H. Wu, L. Chen, S. Su, Y. Cao, *Adv. Mater.* **2011**, 23, 4636.

43 W. Jiang, R. Yu, Z. Liu, R. Peng, D. Mi, L. Hong, Q. Wei, J. Hou, Y. Kuang, Z. Ge, *Adv. Mater.* **2018**, 30, 1703005.

44 C. M. Proctor, M. Kuik, T. Q. Nguyen, *Prog. Polym. Sci.* **2013**, 38, 1941.

45 G. Perrier, R. D. Bettignies, S. Berson, N. Lemaitre, S. Guillerez, *Sol. Energy Mat. Sol. C.* **2012**, 101, 210.

46 Y. Zheng, T. Goh, P. Fan, W. Shi, J. Yu, A. D. Taylor, *ACS Appl. Mater. Interfaces* **2016**, 8, 15724.

47 M.Y. Chiu, U.S. Jeng, C.H. Su, K.S. Liang, K.H. Wei, *Adv. Mater.* **2008**, 20, 2573.

48 E. P. Yao, C. C. Chen, J. Gao, y. Liu, Q. Chen, M. Cai, W. C. Hsu, Z. Hong, G. Li, Y. Yang, *Sol. Energy Mater. Sol. C.* **2014**, 130, 20-26.

49 B. Xiao, M. Zhang, J. Yan, G. Luo, K. Gao, J. Liu, Q. You, H. B. Wang, C. Gao, B. Zhao, X. Zhao, H. Wu, F. Liu, *Nano Energy* **2017**, 39, 478.

50 Y. Yan, F. Cai, L. Yang, J. Li, Y. Zhang, F. Qin, C. Xiong, Y. Zhou, D. G. Lidzey, T. Wang, *Adv. Mat.* **2017**, 29, 1604044.

51 J. Diaz, G. Paolicelli, S. Ferrer; F. Comin, *Phys. Rev. B* **1996**, 54, 8064.

52 M. H. Richter, D. Friedrich, D. Schmeißer, *BioNanoScience* **2012**, 2, 59.